

Classification of anomalies in electroluminescence images of solar PV modules using CNN-based deep learning

Hazem Munawer Al-Otum

EE Department, Faculty of Engineering, Jordan University of Science & Technology, Jordan

ARTICLE INFO

Keywords:

Deep learning
Convolutional neural network
Fault detection and classification
Electroluminescence imaging

ABSTRACT

The escalation of implementing photovoltaic (PV) power generation has paved the road to innovative remarkable applications. The technology of utilizing electroluminescence imaging (EL) has aided the early identification of faults and rapid classification of solar cells in PV panels. Recently, deep learning neural networks (DNNs) has been extensively utilized in the field of PV fault detection and classification. Despite of the good achievements in the field of DNN-based approaches, however, there is still a potential for further developments. This includes better data preparation, proper dataset categorization and designing of efficient light-weight DNNs. In this work, an efficient approach is proposed to be used for defect detection and malfunctions' classification in PV cells, based on utilizing EL-based imaging analysis. Here, three approaches were developed using multi-scale convolutional neural network (CNN) models, the former is based on deploying the pretrained SqueezeNet and the GoogleNet, in a transfer learning fashion, whereas the latter is a light-weight CNN approach (denoted as LwNet). The experiments were elaborated on the ELPV dataset after being properly modified and categorized. Two scenarios were adopted: 4-class- and 8-class-classification procedures. Experimental validation of the developed CNNs have demonstrated very promising performances, especially when adopting the 8-class approach. An average accuracy of about 94.6%, 93.95%, and 96.2% was obtained using GoogleNet, SqueezeNet and LwNet, respectively. A privilege has been granted to LwNet over SqueezeNet and GoogleNet, in terms of classification performance and time saving efficiency.

1. Introduction

Recently, a tremendous development has been witnessed in the field of solar energy based on utilizing technologies of photovoltaics (PV). The huge demand on solar systems is vastly growing and becoming widespread in domestic as well as commercial applications [1–3]. PV modules are widely spread on all continents. According to the report released by the International Energy Agency (AEI), the global PV-based installed systems grew significantly in 2022 [1], reaching about 1,185 GW of installed cumulative capacity according to preliminary market data. The installation of new systems has been increased by about 240 GW with penetration exceeding 10 %. The Chinese market continues to dominate approaching a total capacity of about 414,5 GW, which is more than double that in Europe. European countries have continued a strong growth with 39 GW installed, led by Spain (8,1 GW), Germany (7,5 GW), Poland (4,9 GW) and the Netherlands (3,9 GW). The American market engaged up to 18,6 GW PV capacity, while Brazil nearly doubled its PV systems approaching 9,9 GW. Other countries like India, Korea and Australia have demonstrated a strong growth in PV installations

capacities. Such a tremendous growth urged the demand on developing smart technologies for defect detection and classification in PV systems. This aids the assessment of the operating PV module on site and permits to take proper arrangements while saving labor and time resources [3].

Solar cells today are mostly made of silicon with two types available, the mono- and poly-crystalline cells (denoted as mc-Si and pc-Si, respectively). Their energy conversion efficiency approaches 30 % with a privilege being granted to pc-Si cells [4]. However, these cells may suffer from various anomalies like finger-interruptions, disconnections, cracks, breaks, etc. Such defects can seriously affect the output power of the PV module [4,5]. To evaluate the PV degradation, the characterization methods can be applied using the I–V curve acquisition of the PV module's electric properties. Ultimately, imaging methods like infrared (IR) or electroluminescence (EL) techniques are able to visualize the PV module properties [6].

On the other hand, deep learning has gained a tremendous attention as an efficient approach for detecting and classifying faults in solar cells and PV systems as well. Deep neural networks (DNN) have remarkably pushed the development of detecting and classifying the various PV

E-mail address: hazem-ot@just.edu.jo.

<https://doi.org/10.1016/j.solener.2024.112803>

Received 9 June 2023; Received in revised form 24 June 2024; Accepted 22 July 2024

Available online 27 July 2024

0038-092X/© 2024 International Solar Energy Society. Published by Elsevier Ltd. All rights are reserved, including those for text and data mining, AI training, and similar technologies.

anomalies to another peak. Specifically, convolutional neural network (CNN) approaches were implemented to provide more reliable results in diagnosing these faults [7–22]. In EL imaging, early methods were devoted to the detection of PV faults by classifying the PV panel into healthy or defective without categorizing the defect type. In [7], Bartler et al. generated a dataset, taken from 98,280 cell images, by applying cropping operations on the EL images with a postprocessing stage via distortion-perspective correction. The effect of oversampling and augmentation was developed to override the imbalanced source dataset. Transfer-learning algorithm was deployed in a binary classification mode using the pretrained VGG-16 network [8] with an average accuracy of about 92 %. In [9], Balzategui et al. classified EL images into “degraded” and “non-degraded” categories using a CNN-based model. The approach classified the cells into either flawed or flawless cells. A sliding window was adopted to reduce inadequate data size. Simulations showed an accuracy of about 85 %. In [10], Otamendi et al. utilized multiple data resources and augmentation techniques to develop an end-to-end deep learning pipeline that could detect, locate, and segment PV malfunctions using EL images of the PV cells. Simulations showed good performance with an accuracy of about 84 %. In [11], Prabhakaran et al. proposed an efficient method, denoted as real-time multi variant DNN model (RMVDM), to identify and localize PV panel defects like cracks, micro-cracks, dust accumulation, finger interruptions, and spotlight. The scheme was tested using captured grayscale images of the tested PV panels. In [12], Xie deployed a network with CNN architecture to classify the solar cell into normal or cracked. Here, an attention-based transfer learning, supported with a class-aware domain discriminator, was proposed to improve the performance of the transferred-based CNN model. The proposed approach achieved a good recall of about 84.7 % and a high precision of about 90.2 %.

Other research works pushed the classification of the PV anomalies, based on EL imaging, to another peak. Here, the approaches were developed to detect and classify PV cell defects into various categories. In [13], Karimi et al. proposed an approach to classify EL images of the cells’ defects into corroded, cracked, and good cells. The classification was based on utilizing random forest (RF), support vector machines (SVM) and CNN-based deep learning. In [14], Tang et al. developed data augmentation using a generative adversarial network (GAN) to reduce the effect of imbalanced datasets as well as to avoid overfitting. The utilized dataset contained 4 classes: microcrack, finger-interruption, breakage, and flawless. Results showed that the deployed DNN model exhibited a testing accuracy of about 83 % which was higher than other existing tested models (VGG-16, MobileNet, ResNet-50 and Inception-V3). In [15], Tang et al. utilized a 4-class scenario, with 250 images per class, to classify the EL images. The approach divided the utilized dataset into four classes and applied a CNN-based network with an achieved accuracy of about 92 %. In [16], Lin et al. proposed two light CNN models with resulting precision and recall of around 99.4 % and 98.8 %, respectively. However, the results were obtained using a dataset with only mc-Si type of PV cells.

However, in the prescribed works [13–16], the employed datasets were different which makes the task problem specific, and it would be inadequate to compare the achieved performances. Recently, a well-prepared dataset was published and can be used as a benchmark for visual inspection of PV cells in EL imagery [17]. This dataset is available publicly and was named as ‘ELPV’. Lately, many research works were carried out based on utilizing the ELPV dataset. In [18], Deitsch et al. proposed a CNN-based model for analyzing cells’ defects using their EL images provided by the ELPV dataset. Here, EL images were classified into non-defected, possibly normal, possibly defected and defected. Results showed an average accuracy approaching 88.5 %. In [19], Akram et al. developed a light CNN model, based on utilizing the ELPV dataset, with an achieved accuracy around 93 %. In [20], Demirci et al. proposed an automatic framework that was denoted as deep feature-based (DFB) method. A transfer-based learning approach was deployed by involving VGG-16, VGG-19, DarkNet-19, and ResNet-50

models. Results showed high classification accuracies of around 90.6 % when considering four classes. In [21], Zhao et al. proposed to deploy the high-resolution network (HRNet) for PV defect detection. The approach was based on replacing the classification layer of the HRNet by a proposed self-fusion network (SeFNet). The proposed SeFNet exhibited better performance in terms of the feature fusion of the multi-resolution information in the EL image of the investigated PV models. Another work that utilized the ELPV dataset is the work of Korovin et al. [22]. They proposed an efficient deep-learning-based defect detection and classification model using EL imaging. The introduced model (denoted as SeMaCNN) was based on the concept of the Mahalanobis distance that can be trained using an imbalanced dataset in a semi-supervised mode. The proposed model has accomplished an accuracy and F1-score of about 94.6 %, and F1-score, respectively. However, the number of classes was limited to 2 and 3 during model verification.

A close analysis of the surveyed literature, one may note the followings:

- 1- Different EL image datasets were utilized in various research works. This makes the archived results be problem specific. However, there are few works that were based on using the prescribed published ELPV dataset.
- 2- In most of the previous works, the classification approaches were based on collecting mc-Si and pc-Si cells, having the same features, in the same class. In fact, mc-Si and pc-Si cells have different features (under EL imaging) and this adoption may lead to erroneous sample annotations within each class as well be seen later.
- 3- Despite of the good achievements in the field of DNN-based PV cells’ classification, however, there is still a potential for further developments. Possible directions can be elaborated by a) providing better preparation of the utilized dataset to avoid overfitting, b) organizing proper categorization of the available classes for the anomalies of the PV cells’ defects, and c) designing light-weight CNNs that provide a compromise between DNN classification performance and complexity costs.

Consequently, the current research is oriented toward bridging the gap in research in the field of classification of the PV anomalies. The current research is proposed to deploy CNN-based models for detection and classification of defects in PV cells using EL imaging. The adopted methodology is based on utilizing transfer learning of well-known DNNs and developing a light-weight multi-scale CNN-based model for fault detection and classification.

The remainder of this article is arranged as follows: In Section 2, the concept of the EL imaging and the PV modules is introduced including the adopted ELPV dataset. In section 3, the main methodology is described, in detail, including the modified dataset and the proposed CNN-based models. In section 4, experimental results are elaborated and discussed, while, in section 4, concluding remarks are outlined.

2. EL imaging of the PV modules

2.1. ELPV imaging

EL imaging is a fast and relatively inexpensive technique for spatially resolved and non-destructive analysis of PV modules [23]. Normally, when the cell is forward biased, it emits energy in the wavelength range of 1100-nm range. A specialized CCD-camera is used to capture this emitted energy and construct the so called EL image. Typically, the whole process is elaborated in a dark chamber to ensure a high system resolution [24]. Illustrative examples on EL images are shown in Fig. 1. (randomly selected from ELPV [17]).

Using EL imaging, different types of defects can be recognized in PV cells. This includes cracks, microcracks, finger-interruptions, disconnected cells, diode failure, soldering defects, etc. Such anomalies and defects may diversely affect the PV cell and its normal operation and

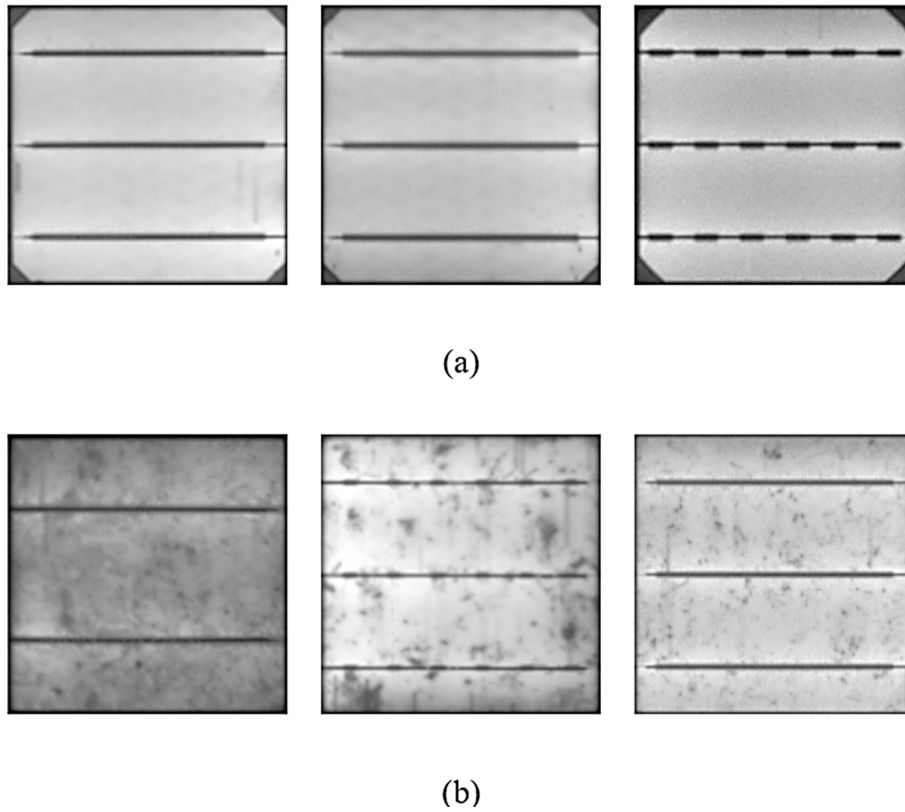


Fig. 1. Selected EL images (from the ELPV dataset) for: a) mc-Si, and b) pc-Si cells.

may lead to create hotspots with severe power loss or even total failure [24]. Consequently, an urging demand is raised to develop automatic procedures for defect inspection and classification using EL imaging systems.

2.2. The ELPV dataset

As prescribed, the ELPV dataset was created by Buerhop-Lutz et al. and is available on their GitHub repository [17]. This dataset contains around 2,624 EL images, about 1116 samples were considered as non-defective, while 1508 samples were considered as defective. The included faults include various types ranging from micro-cracks to totally disconnected cells. Due to the complexity in detecting the precise

degree of the PV defect, the defect likelihood was assigned for each cell according to the anticipated cell damage probability. In ELPV, image samples are categorized into four classes, according to the level of the defect associated with each cell. Thus, the cell annotations were adopted as being (non-defected), 33 % (possibly normal), 66 % (possibly defected) and 100 % (defected). To simplify our task, the prescribed classes were annotated as ND (non-defected), PN (possibly normal), PD (possibly defected) and DF(defected). Fig. 2 depicts the distribution of cells per class in the original ELPV dataset.

3. Methodology

In this work, an efficient approach is proposed to be used for defect

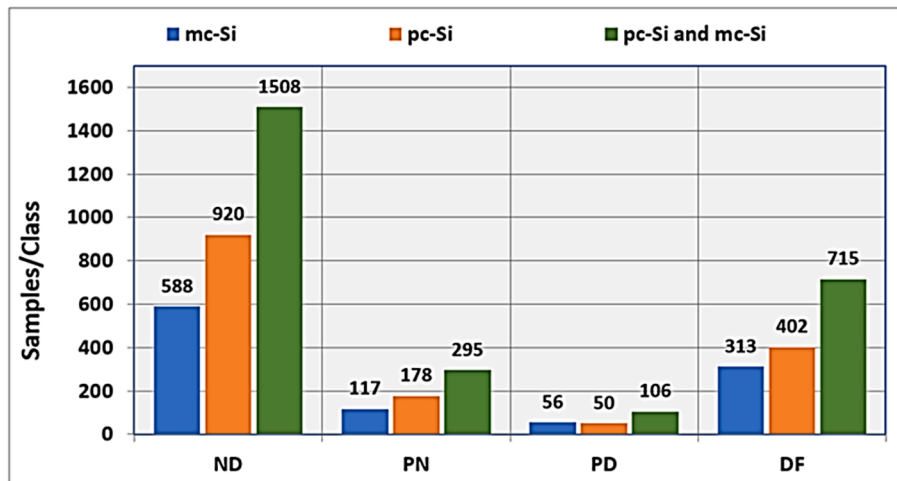


Fig. 2. The distribution of the PV cells per class in the original ELPV dataset.

detection and classification of solar cells, based on utilizing EL imaging analysis. The experiments were elaborated on the ELPV dataset after being modified to override overfitting during training, as well as to properly classify cells (mc-Si and pc-Si) into relative classes. Two scenarios were adopted: a 4-class and 8-class classification approaches. The developed models are based on either transfer-based deployment of pretrained DNNs (SqueezeNet and GoogleNet), or on a developed lightweight CNN approach (denoted as LwNet). The methodology is developed in the following stages: a) preparing the modified balanced ELPV dataset, b) classification of malfunctions in EL Images using the proposed CNN models, and c) evaluation tests of fault detection and classification.

3.1. Preparing the modified ELPV dataset

Referring to the cells' distribution in the original ELPV dataset (Fig. 2), it is clear that:

- the number of samples per class is imbalanced with about 57.5 %, 11.2 %, 4.0 %, and 27.2 % of the total number of samples in ND, PN, PD and DF classes, respectively. However, this imbalanced distribution usually leads to overfitting during the training stage. Evidently, there is a shortage in having large datasets with a balanced number of samples in each class. This situation occurs in most of the practical real-world aspects. when implemented in DNN-based classification models, this creates restrictions to afford high performance. To handle this situation, the ELPV dataset is to be modified to obtain almost balanced number of samples per class using proper data augmentation. Data augmentation aims at increasing the number of samples while preserving its original label. A simple and straightforward procedure for data augmentation is obtained by applying simple image processing operations to each of the input samples. In this work, data augmentation has been performed using various operations like image translation, flipping, rotation, resizing, gray level adjustments, histogram equalization, noise addition, and random cropping.
- Each class contains both mc-Si and pc-Si cells with, again, imbalanced number of samples. In fact, panels made of pc-Si cells are cheaper than that of the mc-Si panels, however, they are less efficient and aren't as aesthetically pleasing. Here, the captured EL images of the pc-Si cells have a grained (dirty) surface due to its internal construction. This is clearly seen when comparing the EL images in Fig. 1.a, and Fig. 1.b. The approach of combining both types of cells in one class may mislead the appropriate classification of cells into proper classes. To accurately tackle this issue, it is advised to split the

mc-Si and pc-Si cells into separate classes that consider the properties of each type of the Si cells.

Considering the prescribed concerns, the ELPV data set has been modified by applying proper augmentation along with splitting the mc-Si and pc-Si samples into separate classes. For instance, the ND class has been split into two subclasses with non-defected mc-Si (mc-ND) and non-defected pc-Si (pc-ND) cells. The other three classes are treated similarly. This produces 8-classes, are annotated as: mc-ND, pc-ND, mc-PN, pc-PN, mc-PD, pc-PD, mc-DF, and pc-DF. The distribution of samples in each class of the modified balanced ELPV dataset is depicted in Fig. 3. Note that the portion of samples per class is about 12.5 %. For comparison purposes, classes with similar anomalies have been recombined to produce a balanced 4-class ELPV dataset with about 25 % of samples per class.

3.2. Classification of malfunctions in EL images using CNN models

Recently, CNNs attracted a great attention in the field of deep learning applications. CNNs are a special type of DNNs that are particularly suited for structured data (like images). CNNs are used for image recognition and various processing tasks. On the other hand, transfer learning approaches can be utilized, where pre-trained CNN models are used as the starting step for another classification task. With transfer learning, a deep learning model can be trained using small datasets because the model has already been pre-trained, hence, the training time can be intensely decreased, when compared to training time consumed on the training stage from scratch. In this work, two approaches are proposed for classification of EL images, the former is based on using a learning-from-scratch approach and is based on developing a lightweight CNN network, whereas the latter is based on transfer learning approach. Here, two pretrained DNNs were selected, one with a medium depth (SqueezeNet), while the other is with a high depth (GoogleNet). These approaches are described below in detail.

3.2.1. LwNet for fault classification in EL images

To meet the tradeoff between DNN efficiency and accuracy, a lightweight multi-scale CNN (LwNet) is proposed. LwNet is inspired by the architectures of SqueezeNet, GoogleNet, and AlexNet [20,25–27]. The main features of the proposed LwNet are based on utilizing the relatively new deep learning components like the leaky relu activation function, the 1x1 convolution layer as well as the dropout unit. Moreover, the architecture of LwNet is constructed of three steps as shown in Fig. 4. At the initial step, the size of the convolution kernels are selected to be relatively small accompanied by the leaky relu activation function to

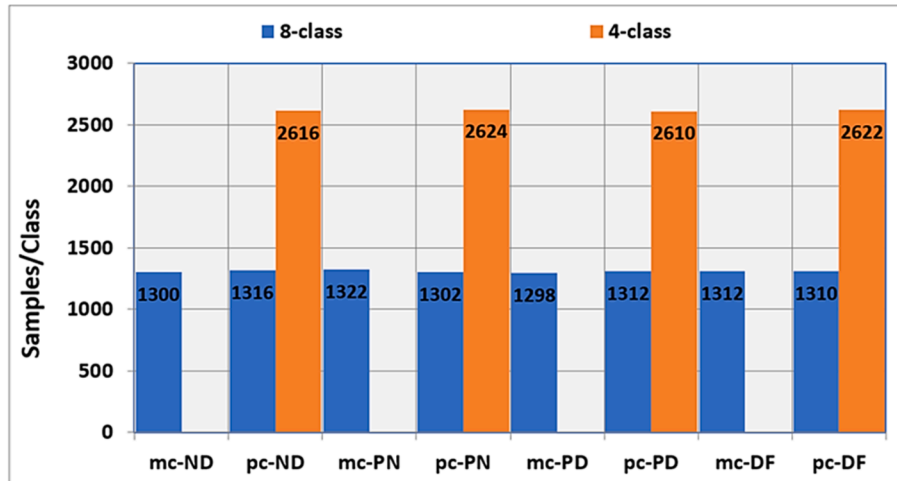


Fig. 3. The distribution of PV cells, per class, in the modified balanced ELPV dataset.

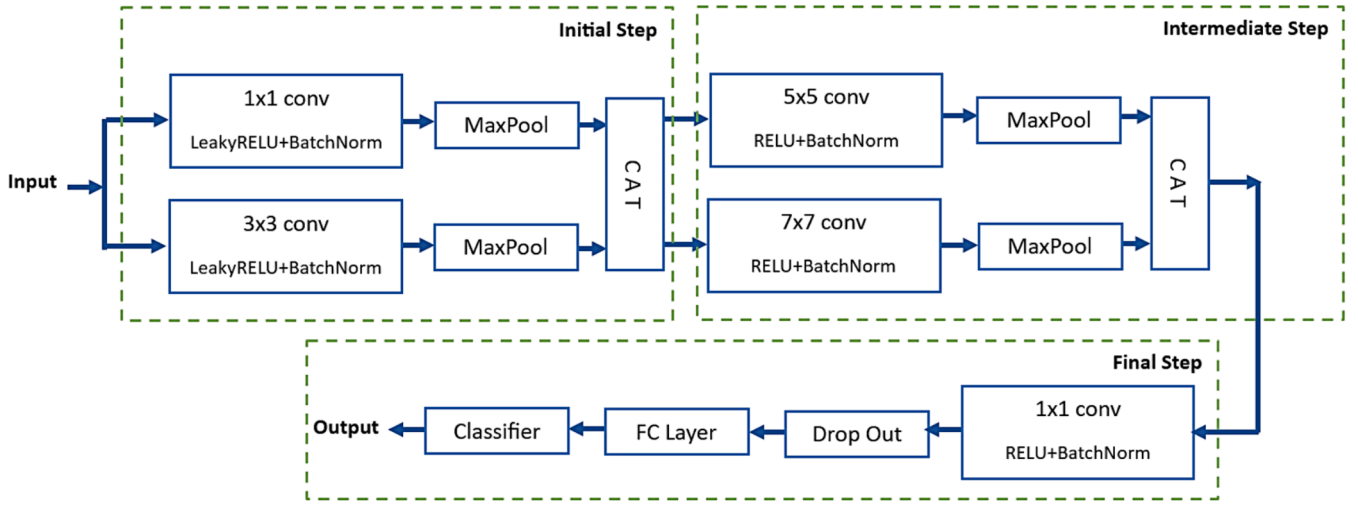


Fig. 4. The block diagram of the proposed LwNet.

capture the tiny features and keep a small portion of the negatively achieved features. This led to enhance the performance of the proposed LwNet. At the intermediate step, convolutional layers have larger kernels to capture more features at a different scale. At the final step, again, 1x1 convolution is reused to confine missed features at the intermediate stage. To speed up the model, a dropout layer is added before using the fully connected layer. These topics are discussed in detail below.

A detailed architecture of the LwNet is depicted in Fig. 5. Clearly, it is constructed of 26 layers, and takes place in three stages: initial, intermediate, and output stages. The proposed LwNet has the following key features:

- 1) LwNet utilizes various types of convolutional filters to aid capturing image features at different scales. Here, two classes of convolutions were adopted, namely:
 - At the initial stage, small-sized convolutional filters (1x1 and 3x3) were used. At this stage, the spatial features are dominating which gives an ability to speed up the suggested network as well as to have a smaller receptive field. Moreover, LwNet utilized the concept of using multiple types of filter, with different sizes, on the same image block (1x1 and 3x3 kernels). This was inspired by the concept of the inception module in the GoogleNet model [25].
 - At the intermediate stage, medium-sized convolutional filters (5x5 and 7x7) were used. This gives privilege to extract features at larger scales. Evidently, features extracted from large kernels would be generic and spread across the image. This concept was inspired by the AlexNet and the GoogleNet models [20,25].
- 2) In LwNet, the conventional relu activation function was replaced by the leaky relu. Actually, the relu activation function can be written as [27]:

$$f(x) = \begin{cases} x, & \text{if } x > 0 \\ 0, & \text{otherwise} \end{cases} \quad (1)$$

While, the leaky relu is adopted to be as [27]:

$$f(x) = \begin{cases} x, & \text{if } x > 0 \\ 0.01x, & \text{otherwise} \end{cases} \quad (2)$$

The insertion of a small negative slope in the leaky relu (Fig. 6), when compared to the relu function (Fig. 6), made it possible to override the “dying ReLU” problem, hence, improving the overall DNN performance.

- 3) A dropout layer has been employed at the final stage of LwNet. Dropout insertion boosts acting on multiple pathways for prediction. When no dropout being utilized, the the forward propagation can be performed according to:

$$\begin{aligned} z_i^{(l+1)} &= w_i^{(l+1)} y_i^l + b_i^{(l+1)} \\ y_i^{(l+1)} &= f(z_i^{(l+1)}), \end{aligned} \quad (3)$$

Where

$z_i^{(l+1)}$ - the i -th output of layer $(l+1)$ before activation

y_i^l - the i -th output of layer l .

$w_i^{(l+1)}$ - the i -th weight of layer $(l+1)$.

$b_i^{(l+1)}$ - the bias of layer $(l+1)$.

$f(\cdot)$ - the used activation function.

While, when the dropout layer is included, these equations will be modified as:

$$r_j^{(l)} \sim \text{Bernoulli}(p)$$

$$\tilde{y}^{(l)} = y^{(l)} * r^{(l)}$$

$$z_i^{(l+1)} = w_i^{(l+1)} \tilde{y}^{(l)} + b_i^{(l+1)}$$

$$y_i^{(l+1)} = f(z_i^{(l+1)}) \quad (4)$$

Where

$r^{(l)}$ - a vector of independent Bernoulli random variables with probability of 1 (at layer (l)).

$\tilde{y}^{(l)}$ - the output of layer (l) obtained as a result of dot multiplication of $y^{(l)}$ of and $r^{(l)}$.

Hence, before calculating the vector z , the input to the layer is multiplied with the independent Bernoulli variables r that act as a mask to the input variable. This leads to keep only a few units according to the dropout rate. The dropout is deployed to prevent overfitting on the training data. When no dropout is used, the initial batch of training excessively influences the whole process, leading to overfitting. At the presence of dropout, the network is encouraged to learn more robust and generalized features. Thus, dropout adds a randomness behaviour during training, which advances the network to rely on multiple pathways for prediction. In LwNet, the dropout layer has a dropout rate of $p = 0.2$, i.e., about 20 % elements of the input tensor, being randomly selected, are set to zero during the training phase. A demonstrative example on the dropout concept is shown in Fig. 7.

In the initial stage, the input image is applied to a parallel combination of convolutional layers (conv1_1 and conv1_2) with a kernel size of 1x1 and 3x3, respectively. As a result, elementary features like shape and boundary can be captured at both 1x1 and 3x3 scales. The outputs of

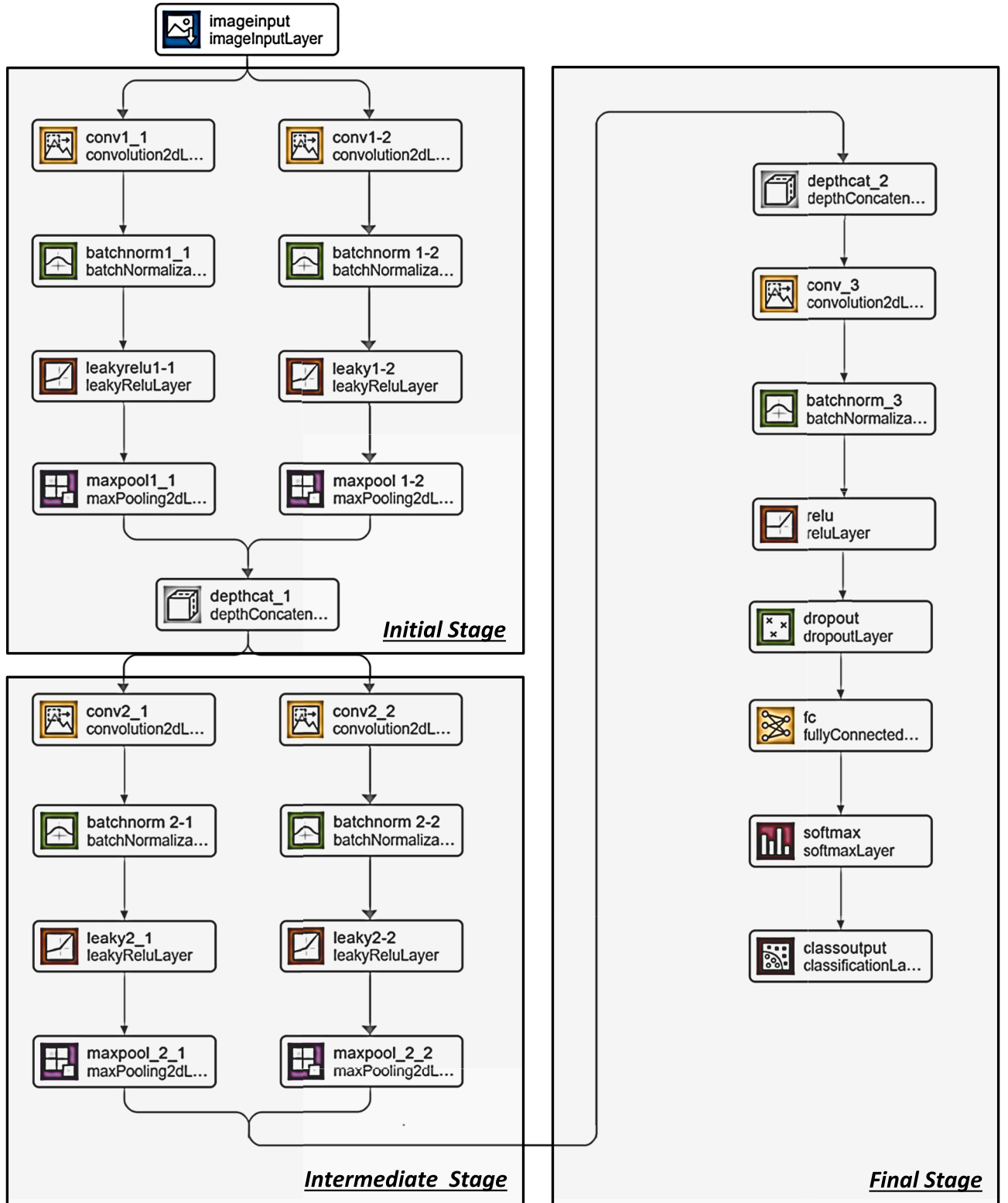


Fig. 5. The block diagram of the proposed LwNet.

these layers are applied to batch normalization layers (batchnorm1_1 and batchnorm1_2) to improve the model performance and stability. By standardizing their outputs, the model learns faster while reducing possible network overfitting. The outputs of batchnorm1_1 and batchnorm1_2 are applied to the activation leaky relu layers (leakyrelu1_1 and leakyrelu1_2), respectively with a constant gradient α (in LwNet $\alpha = 0.1$).

The outputs are applied to maxpooling layers (maxpool1_1 and maxpool1_2) that are used to decrease the dimension of the inputs, coming from leakyrelu1_1 and leakyrelu1_2, based on the statistics of neighboring cells. This leads to extract more learned features and improve the model performance. This stage ends by applying the maxpooling outputs to a depth concatenation layer (depthcat_1) that concatenates the inputs

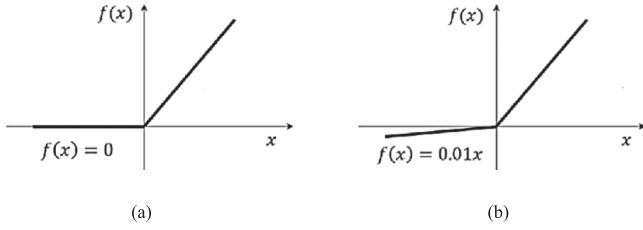


Fig. 6. a) relu, and b) leaky relu activation functions [27].

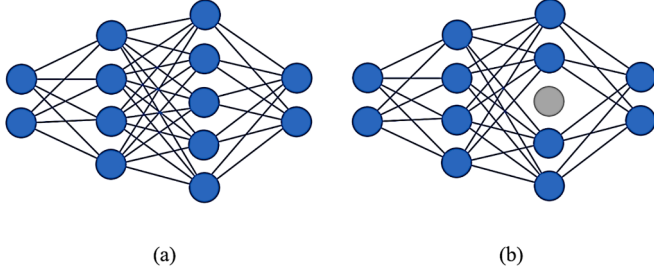


Fig. 7. Demonstrative example on the dropout layer: a) without dropout, b) dropout with a rate of 0.2.

along the channel dimension. On the intermediate stage (see Fig. 5), the concatenated output is applied to parallel convolution layers (conv2_1 and conv2_2) with kernel sizes 7x7 and 5x5, respectively. In fact, the insertion of parallel convolutional branches with various kernel sizes allows to capture a wide variety of features ranging from elementary to specific textures and patterns. Similar to steps taken in the initial stage, the output of the convolutional layers are applied, in a parallel mode, to batch normalization layers (batchnorm2_1 and batchnorm2_2), leaky relu layers (leakyrelu2_1 and leakyrelu2_2 with $\alpha = 0.1$) and maxpooling layers (maxpool2_1 and maxpool2_2), respectively. This stage ends by combining the parallel outputs in the depthcat_2 layer.

At the final stage, the depthcat_2 output is applied, sequentially, to convolutional (conv_3), batch normalization (batchnorm_3), and relu activation (relu_3) layers. Here, conv_3 utilizes a 1x1 kernel for improved fine features extraction. The output of the relu layer is applied to a dropout layer. Here, some of the neurons are dropped or omitted randomly with a dropping rate of 0.2. The insertion of this layer is used to reduce overfitting in DNNs models. Usually, overfitting arises when the size of the available data for training is limited which leads the network to show higher training accuracy than the testing accuracy. Next, fully connected layer (fc) is used to perform the decision step on the LwNet. The fc layer is constructed of a multi-layer perceptron. It can learn weights utilized in categorizing object classes. The output of the fc layer is applied to the softmax activation function which is adopted as the readout layer for multivariate classification tasks. Finally, the output is applied to the classification layer (classoutput) that calculates the loss using the cross-entropy and implies the number of classes from the output size of the previous layer. For more info, the hyperparameters of the proposed LwNet are depicted in Table 1.

3.2.2. Transfer learning-based fault classification in EL images

Transfer learning is a process where a pre-trained DNN model, is retrained on a new problem. Here, one or more layers from the initially trained model are then used in the new DNN model for training on the task of interest. Transfer learning gained popularity in DNNs especially with comparatively little datasets. The adoption of transfer learning leads to a significant drop in the required training and computational power. In this work, two pretrained DNNs were selected in a transfer learning mode to be applied to the ELPV dataset, the former is the SqueezeNet with a medium size having 68 layers, and the latter is the

Table 1
The LwNet hyperparameters.

Layer Type	Parameters	Activations	Learnables
Input Image	246x246x3 pixels		
conv1_1	Size = [3,3], Stride = [1,1], Num of Filters = 16.	246x246x16	Weights: 3x3x3x16 Bias: 1x1x16
conv1_2	Size = [1,1], Stride = [1,1], Num of Filters = 32.	246x246x32	Weights: 1x1x3x32 Bias: 1x1x32
batchnorm_1_1	Epsilon = 0.00001	246x246x16	Offset 1x1x16 Scale 1x1x16
batchnorm_1_2	—	246x246x32	Offset 1x1x32 Scale 1x1x32
leakyrelu_1_1	Scale = 0.1	246x246x16	Offset 1x1x16 Scale 1x1x16
leakyrelu_1_2	Scale = 0.1	246x246x32	Offset 1x1x32 Scale 1x1x32
maxpool_1_1	Poolsize = [2,2], Stride = [2,2]	123x123x16	Offset 1x1x16 Scale 1x1x16
maxpool_1_2	Poolsize = [2,2], Stride = [2,2]	123x123x32	Offset 1x1x32 Scale 1x1x32
depthcat_1	—	123x123x48	Offset 1x1x32 Scale 1x1x32
depthcat_2	—	61x61x16	Offset 1x1x8 Scale 1x1x8
conv2_1	Size = [7,7], Stride = [1,1], Num of Filters = 8	123x123x8	Weights: 7x7x48x8 Bias: 1x1x8
conv2_2	Size = [5,5], Stride = [1,1], Num of Filters = 8	123x123x8	Weights: 5x5x48x8 Bias: 1x1x8
batchnorm_2_1	Epsilon = 0.00001	123x123x8	Offset 1x1x8 Scale 1x1x8
batchnorm_2_2	Epsilon = 0.00001	123x123x8	—
leaky2_1	Scale = 0.1	—	—
leaky2_2	Scale = 0.1	—	—
maxpool_2_1	Poolsize = [2,2], Stride = [2,2]	61x61x8	—
maxpool_2_2	Poolsize = [2,2], Stride = [2,2]	61x61x8	—
conv_3	Size = [1,1], Stride = [1,1], Number of Filters = 32.	61x61x32	Weights: 1x1x16x32 Bias: 1x1x32
batchnorm_3	Epsilon = 0.00001	—	Offset: 1x1x32 Scale: 1x1x32
relu	—	61x61x32	—
dropout	Probability = 0.2	61x61x32	—
fully connected (fc)	Output size = 8 WeightLearnFactor = 10 BiasLearnFactor = 10 WeightL2Factor = 1	1x1x8	Weights: 8x119072 Bias: 8x1
softmax classout (output layer)	Loss function = cross entropy	1x1x8	—

GoogleNet with relatively a high number of layers (144 layers). The details on these DNNs are given below:

1. SqueezeNet: is a DNN designed to be small while being highly accurate. It was developed in 2016 by researchers from DeepScale, UC Berkeley, and Stanford University [24]. SqueezeNet employs a design strategy known as channel squeezing and deep compression to reduce the number of parameters, remarkably with the use of fire modules that “squeeze” parameters using 1x1 convolutions. The main feature of SqueezeNet is that it provides a balance between low complexity and high accuracy, making it an ideal choice for devices with limited resources like embedded systems and mobiles. SqueezeNet is a CNN-based network with a medium number of layers (68) and depth of 18 that can classify images into 1000 object categories. A crucial feature that attracted our attention to deploy the SqueezeNet is its promising architecture, especially in scenarios where computational resources are limited. SqueezeNet is considered as an excellent choice for edge computing scenarios, where both

computational efficiency and high accuracy. This can be attributed to the usage of 1×1 (point-wise) filters, to replace 3×3 filters, in bottleneck fashion to reduce both net depth computational energy, with applying late down-sampling to keep a big feature map. By minimizing computational requirements, it enables AI applications even in resource-constrained environments.

2. GoogleNet: is a DNN designed based on the inception architecture which is used to approximate the CNN optimal local sparse structure. It utilizes various filter types, on a single block of the image, instead of using a single filter size. The utilization of the inception module leads to decrease the number of parameters to only 5 million. It has 144 layers, so it is a very deep network [25].

Undoubtedly, the GoogleNet model provides several key features over previous state-of-the-art winners AlexNet, ZF-Net, and VGG architectures [20,25]. GoogleNet exhibits significant decrease in error rate. Again, the utilization of 1×1 convolutions leads to parameter reduction and depth increase as well. Moreover, GoogleNet employs global average pooling to replace the fully connected layers at the network end. Here, a distinctive feature of GoogleNet is the embedding of the so-called inception module, where the 1×1 , 3×3 , 5×5 convolutions, and 2×2 max pooling are stacked together to generate the final output. This approach allows the network to handle objects at multiple scales effectively.

It is worthy to note that the main reasons behind selecting the SqueezeNet and GoogleNet for EL image classification is attributed to a) the superior trade-off between classification capabilities and computational power, b) the feasibility to be trained on a single-GPU computer, and c) up to our knowledge, neither SqueezeNet nor GoogleNet was deployed for EL image classification using the ELPV dataset.

4. Experimental results and discussion

4.1. Preparations

In this section, the transfer-based learned SqueezeNet, GoogleNet along with the proposed LwNet models are tested using several experiments. Conducted experiments were carried out using a computer with Intel(R) Core(TM) i7-10510U CPU @ 2.30 GHz., 16 GB RAM memory with NVIDIA GeForce MX250 graphics unit (single-GPU). The tests were executed using the Deep Learning Toolbox in MATLAB® R2020a. Here, the amount of training data used for validation is 20 % of the prescribed modified ELPV dataset during the training stage. The prescribed DNNs were trained with Stochastic Gradient Descent (SGD) optimizer with a learning rate $\eta = 10^{-4}$. The proposed LwNet was trained using 50 epochs, while only 30 epochs were assigned to train the pretrained SqueezeNet and GoogleNet. Table.2 lists the training parameters utilized in the evaluations.

4.2. Evaluation metrics

To evaluate the performance of the prescribed DNNs, four metrics were utilized, namely: the accuracy, precision, recall and F1-score. The

accuracy is a measure of the DNN performance among all classes. The precision reflects the percentage of the predicted faults that were classified properly, The recall determines the percentage of the actual faults that were correctly categorized, while F1-score defines the harmonic mean of precision and recall. These metrics are [20]:

$$\text{Accuracy} = \frac{TP + TN}{TP + TN + FP + FN} \quad (5)$$

$$\text{Precision} = \frac{TP}{TP + FP} \quad (6)$$

$$\text{Recall} = \frac{TP}{TP + FN} \quad (7)$$

$$\text{F1-score} = 2 \frac{P \times R}{P + R} \quad (8)$$

Where, TP, TN, FP, and FN denote the true positives, true negatives, false positives, and false negatives, respectively.

4.3. Results for classification of anomalies in EL images using the 4-Class method

In this section, a 4-class approach is investigated. As prescribed, mc-Si and pc-Si cells, with similar anomalies have been combined to produce 4 classes (denoted as ND,PN,PD and DF) in the modified balanced ELPV dataset with about 25 % of samples per class. In fact, this classification scenario was adopted by other researchers in previous works (for instance, in [14,18,20]). The obtained experimental results for the tested DNNs are illustrated in Fig. 8 for the accuracy (Fig. 8.a), precision (Fig. 8.b), recall (Fig. 8.c), and F1-score (Fig. 8.d). In Fig. 8.a-d, the average values (for all classes) are also depicted.

4.4. Results for classification of anomalies in EL images using the 8-class method

The current test was conducted by splitting the dataset into 8-classes depicted in Fig. 3. The mc-Si and pc-Si cells, with similar anomalies, were split into separate classes. The obtained experimental results for the tested DNNs are illustrated in Fig. 9 for the accuracy (Fig. 9.a), precision (Fig. 9.b), recall (Fig. 9.c), and F1-score (Fig. 9.d). In Fig. 9.a-d, the average values (for all classes) are also depicted.

To investigate the classification performance in case of simultaneous existence of mc-Si or pc-Si cells, it would be useful to demonstrate the results for the accuracy and F1-score as shown in Table.3. For better comparison, the last column illustrates these metrics in case of the existence of both mc-Si and pc-Si cells based on the 8-class scenario.

4.5. Discussions and comparisons

In this section, the achieved faults' classification results are assessed and compared with results obtained using other, recently published, works. Moreover, recommendations are given with demonstrative examples on the achieved classification performance.

4.5.1. Results' analysis and discussion

Analyzing the performed tests on the prescribed DNNs (Fig. 8 and Fig. 9), one may note that:

- When adopting the 4-class method for classification, a moderate accuracy has been achieved using the prescribed DNNs. In case of using the 4-class approach, average accuracies around 73.62 %, 85.13 % and 85.47 % were achieved using GoogleNet, SqueezeNet and LwNet, respectively.
- In case of adopting the 8-class classification method, the average accuracy has been increased to be 94.56 %, 93.95, and 96.21 % using GoogleNet, SqueezeNet and LwNet, respectively. All prescribed nets

Table 2

Adopted training parameters.

Parameter	Proposed LwNet	SqueezeNet	Google Net
Number of Classes	4 vs. 8	4 vs. 8	4 vs. 8
Used Solver	SGDM	SGDM	SGDM
Inti. Learn. R.	0.0001	0.0001	0.0001
Valid. Frequency	10	10	10
Max Epochs	50	30	30
Mini Batch	64	64	64
L2Norm	10^{-4}	10^{-4}	10^{-4}
Grad. Th. Meth.	L2Norm	L2Norm	L2Norm
Layers	26	68	144

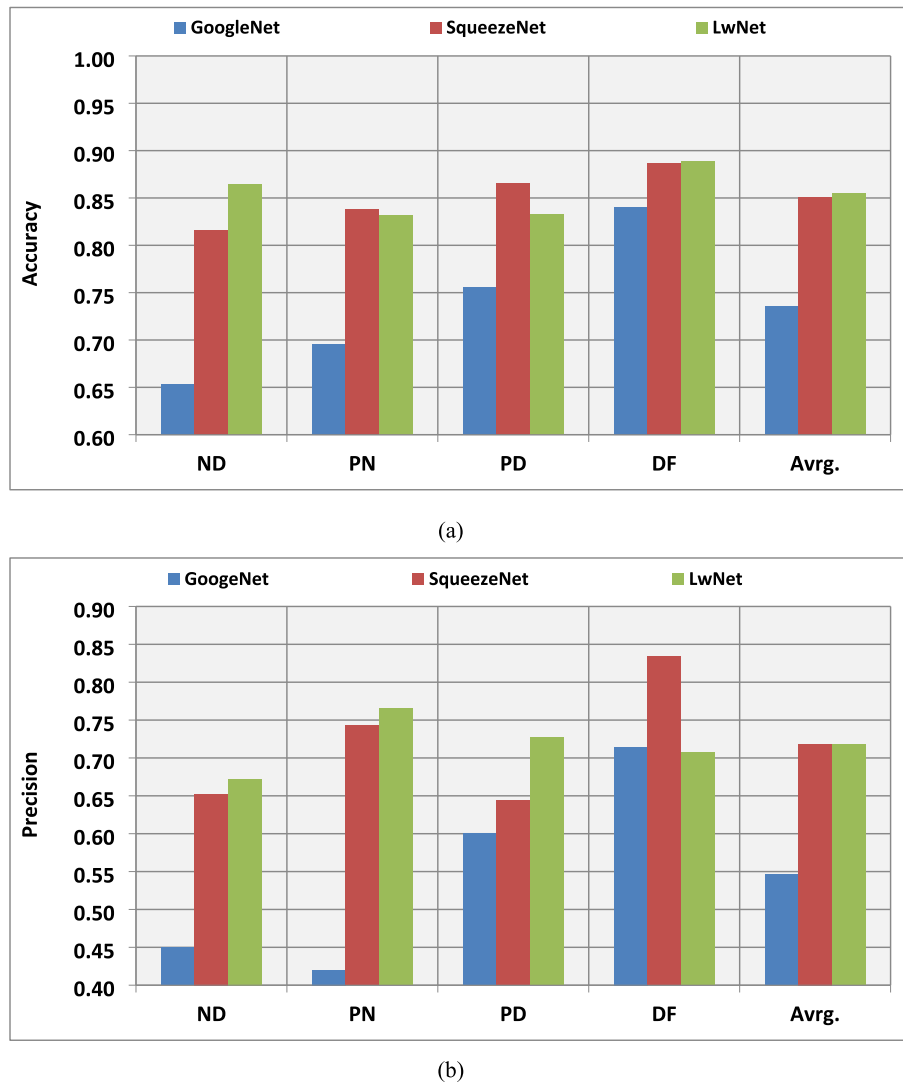


Fig. 8. Experimental results of EL images' anomalies (using the 4-class method) for the tested DNNs in terms of the: a) Accuracy, b) Precision, c) Recall, and d) F1-score.

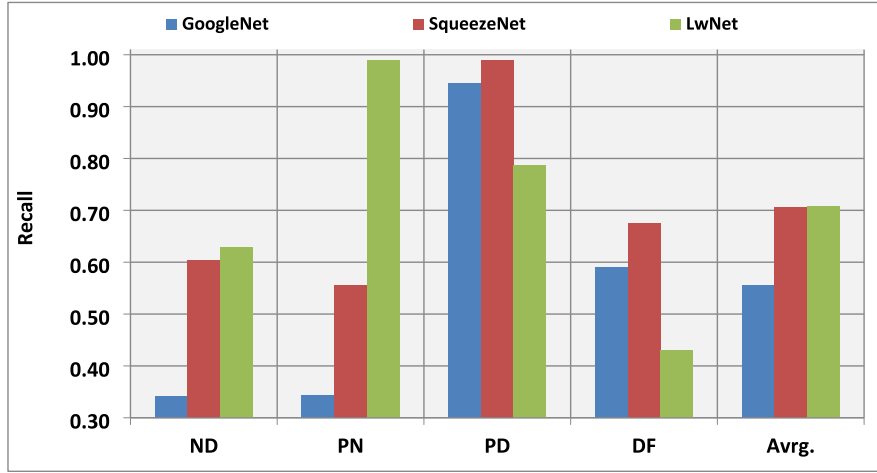
performed excellent when adopting the proposed 8-class method with a privilege granted to the proposed LwNet.

- When considering the other three evaluation metrics, it is easy to reach a similar conclusion that indicates the advantage of using the proposed 8-class approach. For better understanding and visualization, these metrics are depicted with improvement percentage in Table.4. Clearly, the LwNet exhibits almost stable performance in respect to the precision, recall and F1-score. Moreover, there is a clear and good improvement, in all the four evaluation metrics, when using the 8-class method over what is possible using the 4-class method (ranging from 8.8 to 21.0 % according to the used DNN). This can be attributed to the fact that the splitting of the EL images of the solar cells into mono and poly classes led to extract the tiny difference between m-Si and p-Si cells with operational anomalies. Despite that these recommendations are valid for the ELPV dataset, they can also be generalized to other EL image datasets.
- When considering only one type of solar cells (either mc-Si or pc-Si), results indicated that the performance (in terms of the accuracy and F1-score) is higher in case of the simultaneous existence of the mc-Si cells (see Table.3). In case of the simultaneous existence of the pc-Si cell, results were slightly reduced. This is attributed to the better mc-Si cells' surface clarity which enabled the DNN to attain better

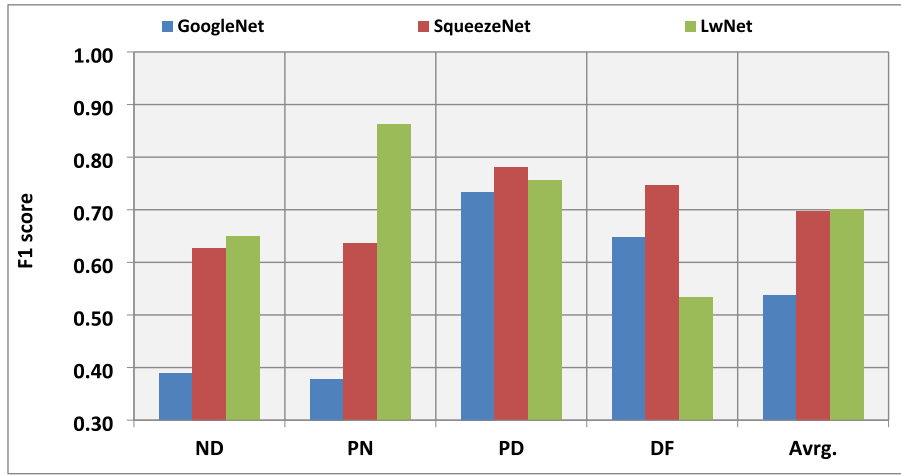
classification. Clearly, results in case of the existence of both types is the average from both types.

4.5.2. Comparison of the computational energy

Apparently, the training of a DNN model is a time-consuming procedure. Generally speaking, the associated operations required for training modern DNNs outpaces the computational capabilities, especially when GPU are exhaustively utilized. To compare the required computational power, the prescribed DNNs were trained using MATLAB.2020.a software on a computer with a single GPU (see section 3.1). The average normalized elapsed time for both 4-class and 8-class approaches is depicted in Table.4. Clearly, the 4-class method consumed slightly higher time than the 8-class method (2 %-6%) for all the prescribed DNNs which strengthens the proposition of adopting the 8-class method for classification. Moreover, GoogleNet consumed the highest elapsed time with SqueezeNet came in the second position. The proposed LwNet consumed the lowest computational time with a reduction of about 40 % of the maximum time consumed to perform training using GoogleNet. This was expected, due to the fact that LwNet is a lightweight DNN. When considering the obtained highest LwNet average accuracy, it is proper to recommend adopting the LwNet as a superior network for EL image classification.



(c)



(d)

Fig. 8. (continued).

For a better understanding, it is worthy to note that the elapsed time consumed to train the GoogleNet model, in case of the 4-class scenario, was 336 min, and 45 s. This is the highest time consumption among all trained DNNs (see Table.5). Nevertheless, the whole training process is usually performed offline before the actual utilization of the trained network.

4.5.3. Illustrative examples

For better illustrations, Table.6 depicts demonstrative examples on the predicted labels of randomly selected samples (from the testing dataset). The random selection of samples was adopted just to show the DNNs performance and, of course cannot be used to give an overall judgment. Nevertheless, the number of misclassified samples is obvious (in case of the 4-class method), also, the erroneous classification is also noticeable with the GoogleNet.

4.5.4. Comparative assessment

To demonstrate the validity of implementing the prescribed DNNs, the achieved results are compared with state-of-art DNN models. For reasonable analysis, the comparative assessments were performed with works that utilized the ELPV dataset. Proper examples are the DNNs presented in [14,18,20,22]. Comparisons are provided in Table.7. Here, works in [14,18,20] utilized a 4-class classification mode, while the work in [22] utilized 3-class scenario (named as A, B and C).

Up to or knowledge, no prior works were elaborated using an 8-class

model. Analyzing Table.7, its clear that the prescribed DNNs exhibited better performance (except for the recall in [20]). Furthermore, the assumption of using the 8-class approach (with the ELPV dataset) led to outstand other compared existing models which fortifies the proposed idea of this research.

4.5.5. Research contributions and recommendations

The main contributions of this work can be outlined in the following:

- 1- Developing an efficient light-weight multi-scale CNN model to be utilized for malfunctions' detection and classification in EL images (denoted as LwNet). The proposed LwNet exhibited an excellent accuracy performance in classifying faults in EL images and provided a compromise solution in terms of the performance and the computational cost.
- 2- Adopting CNN-based models for defect classification in PV cells by utilizing DNN transfer-based learning. Here, two interesting DNN models were elaborated and assessed (GoogleNet and SqueezeNet). The deployed transfer-based GoogleNet and SqueezeNet have shown high performance in detecting and classifying PV faults in EL images with a privilege granted to SqueezeNet in terms of the required computational efficiency.
- 3- Implementing appropriate augmentation of the available ELPV dataset followed by accurate sample labeling along with proper categorization of the samples in the ELPV dataset into proper classes.

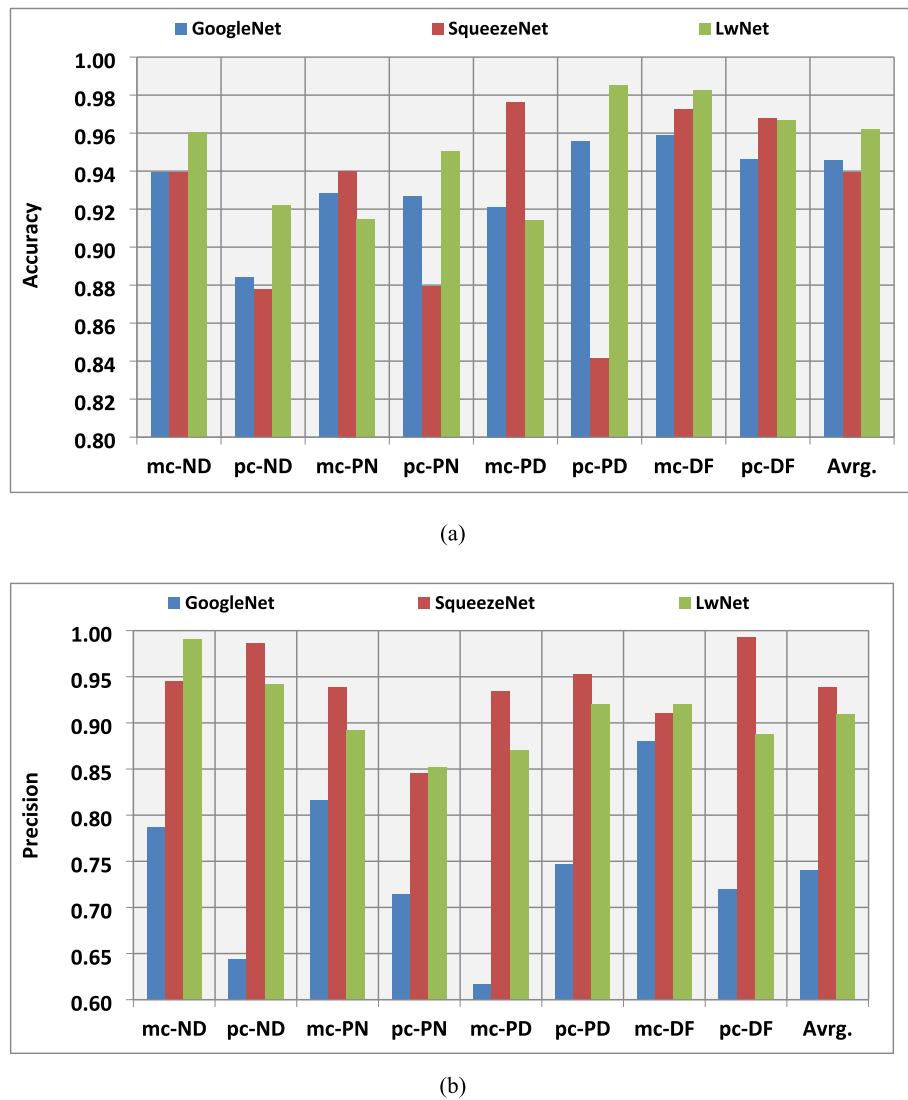


Fig. 9. Experimental results of EL images' anomalies (using the 8-class method) for the tested DNNs in terms of the: a) Accuracy, b) Precision, c) Recall, and d) F1-score.

These procedures led to reach high classification performance including the accuracy, the precision, recall and F1-score.

Finally, it would be worthy to note that the obtained results can be extended to other datasets of EL images and to possibly include other EL images' anomalies. Furthermore, it could be valuable to extend the research results to other issues like thermographic fault diagnosis in commutators and induction motors. This can be tackled in forthcoming papers.

5. Conclusions

The escalation of implementing the deep learning approaches in various aspects of our modern life has paved the way to novel disruptive applications. An increasing growth in the utilization of CNN-based neural networks has been witnessed in the field of PV fault detection and classification. In this work, an efficient defect detection and classification approach, of EL images in PV cells, is developed based on using multi-scale CNN models. Here, two approaches were deployed, the former is based on deploying the pretrained SqueezeNet and the GoogleNet in a transfer learning fashion, whereas the latter is a light-weight

CNN approach (denoted as LwNet). The deployed LwNet, SqueezeNet and Google Net have various number of layers (26, 68 and 144, respectively). The experiments were elaborated on the ELPV dataset after being properly modified and categorized. Two scenarios were adopted, the former, using a 4-class classification procedure, while the latter by utilizing an 8-class classification procedure. Experimental validation of the prescribed DNNs has demonstrated very promising performance, especially when adopting the 8-class approach (which was not tested before). A small privilege has been granted to LwNet over SqueezeNet and GoogleNet in terms of the accuracy, precision, recall and F1-score with a moderate privilege being granted to LwNet in terms of the time saving efficiency.

6. Declaration of generative AI and AI-assisted technologies in the writing process

Statement: During the preparation of this work the author did not use any of the Generative AI and AI-assisted technologies in the writing process of this manuscript.

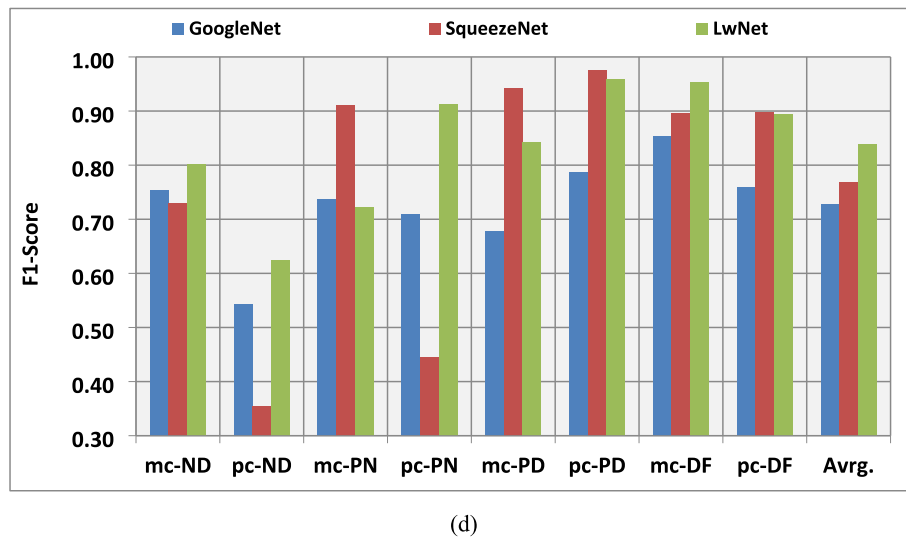
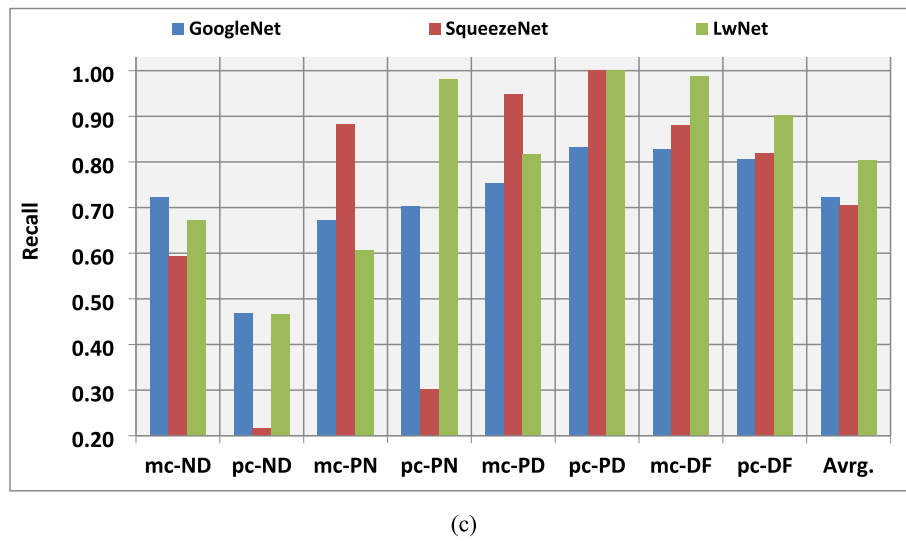


Fig. 9. (continued).

Table 3

Evaluation of simultaneous existence of one type of solar cells.

Targeted Cells	Accuracy			F1-Score		
	GoogleNet	SqueezeNet	LwNet	GoogleNet	SqueezeNet	LwNet
Only mc-Si	0.94005	0.97435	0.9483	0.7554	0.8692	0.8298
Only pc-Si	0.9511	0.9046	0.97595	0.6997	0.6682	0.8472
mc-Si and pc-Si	0.94558	0.93948	0.96213	0.7276	0.7687	0.8385

Table 4

Evaluation metrics improvement percentage for the prescribed Nets.

Scenario	Accuracy			Precision			Recall			F1-score		
	Lw-Net	Squeeze-Net	Google-Net	Lw-Net	Squeeze-Net	Google-Net	Lw-Net	Squeeze-Net	Google-Net	Lw-Net	Squeeze-Net	Google-Net
4-class	0.855	0.851	0.736	0.718	0.718	0.546	0.709	0.706	0.555	0.701	0.697	0.537
8-class	0.962	0.939	0.946	0.903	0.939	0.741	0.903	0.818	0.723	0.839	0.769	0.728
Improvement	10.7%	8.8%	21.0%	18.5%	22.0%	19.5%	19.4%	11.2%	16.8%	13.78	7.1%	19.1%

Table 5

Normalized training time for the tested nets.

Approach	Proposed Lw-Net	SqueezeNet	GoogleNet
4-class	42.4 %	44.1 %	100.0 %
8-class	39.8 %	41.7 %	96.4 %
Time Saving	2.6 %	2.4 %	3.6 %

7. Ethical rules

Hereby, I Prof, Hazem A. Al-Otum consciously assure that for the manuscript:(Automatic Defect Detection and Classification in Electroluminescence Images of PV Cells Using Convolutional Neural Networks), the following is fulfilled:

- 1) This material is the authors' own original work, which has not been previously published elsewhere.

Table 6

Demonstrative results of EL image Classifications.

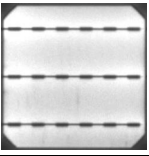
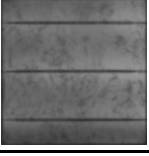
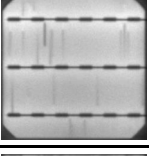
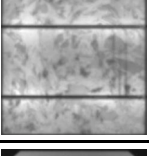
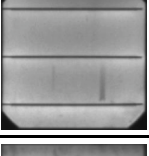
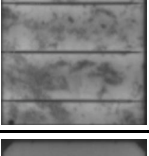
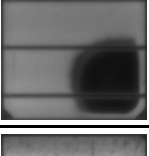
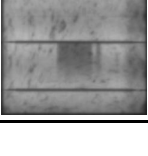
#	EL image	True Label		Predicted Label					
				LwNet		SqueezeNet		GoogleNet	
		8-classes	4-classes	8-classes	4-classes	8-classes	4-classes	8-classes	4-classes
1		mc-ND	ND	✓	✓	✓	✓	✓	✓
2		pc-ND	ND	✓	✓	✓	✓	✓	✗
3		mc-PN	PN	✓	✓	✓	✗	✓	✓
4		pc-PN	PN	✓	✗	✓	✗	✓	✗
5		mc-PD	PD	✓	✓	✗	✓	✓	✓
6		pc-PD	PD	✓	✗	✓	✗	✗	✗
7		mc-DF	DF	✓	✓	✓	✓	✓	✓
8		pc-DF	DF	✓	✓	✓	✓	✓	✗

Table 7

Comparison of DNNs classification performance.

Network Name	# of Classes	Accuracy	Precision	Recall	F1-score
Tang et. al., [14]	4	0.830	—	—	—
Deitsch et. al., [18]	4	0.884	—	—	0.889
Demirci et. al., [20]	4	0.826	0.807	0.916	0.858
Korovin et. al., [22]	3	0.852	—	—	0.888
LwNet	4	0.855	0.718	0.709	0.701
SqueezeNet	4	0.851	0.718	0.706	0.697
GoogleNet	4	0.736	0.546	0.555	0.537
LwNet	8	0.962	0.903	0.903	0.839
SqueezeNet	8	0.939	0.939	0.818	0.769
GoogleNet	8	0.946	0.741	0.723	0.728

- The paper is not currently being considered for publication elsewhere.
- The paper reflects the authors' own research and analysis in a truthful and complete manner.
- The results are appropriately placed in the context of prior and existing research.
- All sources used are properly disclosed.
- All authors have been personally and actively involved in substantial work leading to the paper and will take public responsibility for its content.

Data availability statement

This is to state that the datasets generated and/or analyzed during the current study are available from the corresponding author on reasonable request.

CRedit authorship contribution statement

Hazem Munawer Al-Otum: Conceptualization, Formal analysis, Investigation, Methodology, Software.

Declaration of competing interest

The authors declare that they have no known competing financial interests or personal relationships that could have appeared to influence the work reported in this paper.

References

- https://iea-pvps.org/wp-content/uploads/2023/04/IEA_PVPS_Snapshot_2023.pdf
- <https://www.statista.com/statistics/1394199/global-renewable-capacity-by-source/>
- Global trends for solar in 2023 – pv magazine International (pv-magazine.com).
- A. Fell, K.R. McIntosh, P.P. Altermatt, G.J. Janssen, R. Stangl, A. Ho-Baillie, M. D. Abbott, Input parameters for the simulation of silicon solar cells in 2014, *IEEE J. Photovoltaics* 5 (4) (2015) 1250–1263.
- M. Aghaei, A. Fairbrother, A. Gok, S. Ahmad, S. Kazim, K. Lobato, J. Kettle, Review of degradation and failure phenomena in photovoltaic modules, *Renew. Sustain. Energy Rev.* 159 (2022) 112160.
- L. Koester, S. Lindig, A. Louwen, A. Astigarraga, G. Manzolini, D. Moser, Review of photovoltaic module degradation, field inspection techniques and techno-economic assessment, *Renew. Sustain. Energy Rev.* 165 (2022) 112616.
- A. Bartler, L. Mauch, B. Yang, M. Reuter, L. Stoicescu, Automated detection of solar cell defects with deep learning, 2018 26th European Signal Processing Conference, 2018: 2049–2053.
- K. Simonyan, A. Zisserman, Very deep convolutional networks for large-scale image recognition, *arXiv preprint arXiv:1409.1556*, 2014.
- J. Balzategui, L. Eciolaza, N. Arana-Arexolaleiba, J. Altube, J.-P. Aguerre, I. Legarda-Ereno, A. Apraiz, Semi-automatic quality inspection of solar cell based on Convolutional Neural Networks, 24th IEEE Int. Conference on Emerging Technologies and Factory Automation, 10–13 Sept. 2019, Zaragoza, Spain.
- U. Otamendi, I. Martinez, M. Quartulli, I.G. Olaizola, E. Viles, W. Cambarau, Segmentation of cell-level anomalies in electroluminescence images of photovoltaic modules, *Sol. Energy* 220 (2021) 914–926.
- S. Prabhakaran, R. Uthra, J. Preetharoselyn, Deep learning-based model for defect detection and localization on photovoltaic panels, *Comput. Syst. Sci. Eng.* 44 (2023) 2683–2700.
- X. Xie, G. Lai, M. You, J. Liang, B. Leng, Effective transfer learning of defect detection for photovoltaic module cells in electroluminescence images, *Sol. Energy* 250 (2023) 312–323.
- A.M. Karimi, J.S. Fada, M.A. Hossain, S. Yang, T.J. Peshek, J.L. Braid, R.H. French, Automated pipeline for photovoltaic module electroluminescence image processing and degradation feature classification, *IEEE J. Photovolt.* 9 (5) (2019) 1324–1335.
- W. Tang, Q. Yang, K. Xiong, W. Yan, Deep learning based automatic defect identification of photovoltaic module using electroluminescence images, *Solar Energy*, 201(November 2019), 2020, 453–460. [10.1016/j.solener.2020.03.049](https://doi.org/10.1016/j.solener.2020.03.049).
- W. Tang, Q. Yang, W. Yan, Deep learning based model for Defect Detection of Mono-Crystalline-Si Solar PV Module Cells in Electroluminescence Images Using Data Augmentation, 2019 IEEE PES Asia-Pacific Power and Energy Engineering Conference (APPEEC), 1–4 Dec. 2019, Macao.
- K.M. Lin, H.H. Lin, Y.T. Lin, Development of a CNN-based hierarchical inspection system for detecting defects on electroluminescence images of single-crystal silicon photovoltaic modules, *Mater. Today Commun.* 103796 (2022).
- C. Buerhop-Lutz, S. Deitsch, A. Maier, F. Gallwitz, S. Berger, B. Doll, C.J. Brabec, A benchmark for visual identification of defective solar cells in electroluminescence imagery. In 35th European PV Solar Energy Conference and Exhibition (Vol. 12871289), 2018, September.
- S. Deitsch, V. Christlein, S. Berger, C. Buerhop-Lutz, A. Maier, F. Gallwitz, C. Riess, Automatic classification of defective photovoltaic module cells in electroluminescence images, *Solar Energy*, 185(February), 2019, 455–468. <https://doi.org/10.1016/j.solener.2019.02.067>.
- M.W. Akram, G. Li, Y. Jin, X. Chen, C. Zhu, X. Zhao, A. Ahmad, CNN based automatic detection of photovoltaic cell defects in electroluminescence images, *Energy* 189 (2019) 116319.
- M.Y. Demirci, N. Bešli, A. Gümüşçi, Efficient deep feature extraction and classification for identifying defective photovoltaic module cells in Electroluminescence images, *Expert Syst. Appl.* 175 (2021) 114810.
- X. Zhao, C. Song, H. Zhang, X. Sun, J. Zhao, HRNet-based automatic identification of photovoltaic module defects using electroluminescence images, *Energy* 126605 (2023).
- A. Korovin, A. Vasilev, F. Egorov, D. Saykin, E. Terukov, I. Shakhrai, Zhukov, S. Budenny, Anomaly detection in electroluminescence images of heterojunction solar cells, *Sol. Energy* 259 (2023) 130–136.
- T. Fuyuki, H. Kondo, Y. Kaji, T. Yamazaki, Y. Takahashi, Y. Uraoka, One shot mapping of minority carrier diffusion length in polycrystalline silicon solar cells using electroluminescence, 1343–1345, 2005. [10.1109/pvsc.2005.1488390](https://doi.org/10.1109/pvsc.2005.1488390).
- T. Lai, B.G. Potter, K. Simmons-Potter, Electroluminescence image analysis of a photovoltaic module under accelerated lifecycle testing, *Appl. Opt.* 59 (22) (2020) G225–G233.
- F.N. Iandola, S. Han, M.W. Moskewicz, K. Ashraf, W.J. Dally, K. Keutzer, SqueezeNet: AlexNet-level accuracy with 50x fewer parameters and < 0.5 MB model size, 2016, *arXiv preprint arXiv:1602.07360*.
- C. Szegedy, W. Liu, Y. Jia, P. Sermanet, S. Reed, D. Anguelov, A. Rabinovich, Going deeper with convolutions, in: *Proceedings of the IEEE Conference on Computer Vision and Pattern Recognition*, 2015, pp. 1–9.
- S. Nitish, Dropout: a simple way to prevent neural networks from overfitting, *J. Mach. Learn. Res.* 15 (2014) 1.